European Journal of Materials

ISSN: (Print) (Online) Journal homepage: https://www.tandfonline.com/loi/tems20

Effect of helium as process gas on laser powder bed fusion of Ti-6Al-4V studied with operando diffraction and radiography

Camille Pauzon, Steven Van Petegem, Eduard Hryha, Cynthia Sin Ting Chang, Samy Hocine, Helena Van Swygenhoven, Charlotte de Formanoir & Sophie Dubiez-Le Goff

To cite this article: Camille Pauzon, Steven Van Petegem, Eduard Hryha, Cynthia Sin Ting Chang, Samy Hocine, Helena Van Swygenhoven, Charlotte de Formanoir & Sophie Dubiez-Le Goff (2022): Effect of helium as process gas on laser powder bed fusion of Ti-6Al-4V studied with operando diffraction and radiography, European Journal of Materials, DOI: 10.1080/26889277.2022.2081622

To link to this article: https://doi.org/10.1080/26889277.2022.2081622

Accepted author version posted online: 24 May 2022.

Effect of helium as process gas on laser powder bed fusion of Ti-6Al-4V studied with operando diffraction and radiography

Camille Pauzon[1*], Steven Van Petegem[2], Eduard Hryha[1], Cynthia Sin Ting Chang[2,3], Samy Hocine[2,4], Helena Van Swygenhoven[2,4], Charlotte de Formanoir[5], and Sophie Dubiez-Le Goff[6]

[1]Industrial and Materials Science, Chalmers University of Technology, Göteborg, Sweden,

[2]Photons for Engineering and Manufacturing, Paul Scherrer Institute, Villigen PSI, Switzerland,

[3]ANAXAM, PARK INNOVAARE: deliveryLAB, Villigen, Switzerland

[4]Neutrons and X-rays for Mechanics of Materials, IMX, Ecole Polytechnique Fédérale de Lausanne, Lausanne, Switzerland,

[5]Ecole Polytechnique Fédérale de Lausanne, Lausanne, Switzerland,

[6]Linde GmbH, Unterschleißheim, Germany,

[*]camillepauzon@gmail.com

ABSTRACT

The utilisation of helium as process gas in laser powder bed fusion (LPBF) limits the generation of Ti-6Al-4V hot and incandescent spatters and enhances their cooling rate. In the present study, operando X-ray diffraction using synchrotron X-rays permits to verify that the cooling rates experienced by the deposited material are not significantly affected by the process gas unlike spatters. Topography measurements of the top printed surface reveal lower roughness of He-produced samples, attributed to the previously observed reduction of spatters with He and thus a reduction of redepositions on the powder bed and printed surfaces. Operando radiography provides with insights on the spatter formation mechanisms namely particle entrainment, agglomeration, melting and spheroidization.

HIGHLIGHTS

- The top surface average roughness of samples produced with He is lower than that of Ar equivalent
- Deposited Ti-6Al-4V cooling rates during LPBF are not significantly affected by the use of He
- Grain size and orientation of Ti-6Al-4V is similar when processing under Ar, He, and a mixture of both
- Operando radiography permits to identify the mechanisms of Ti-6Al-4V spatter formation

Keywords: Laser powder bed fusion; Operando X-ray diffraction; Operando radiography; process gas; Spatters; Helium

1. Introduction

The use of helium and addition of helium to the laser powder bed fusion (LPBF) process gas has been investigated in the last 5 years on industrial- and laboratory-developed printers. The drive to extend the process gas portfolio is somehow connected to the welding background, for which dedicated shielding gas recipes have been developed for specific purposes, such as improving arc stability or weld penetration. Because LPBF typically operates with smaller laser spot sizes, higher

scanning speeds, and different laser types than welding, the welding shielding gases are not directly applicable or of interest to LPBF. For example, plasma formation during laser welding using CO_2 lasers (with wavelength 10.6 μm) can be minimised using helium thanks to its high ionization energy, yielding enhanced laser absorption by the material. However for Nd:YAG or Yb-fiber lasers typically used in LPBF, plasma formation and the associated inverse Bremsstrahlung absorption is not as important [1]. Helium is still an interesting starting point of investigation as it is inert like the standardly used argon, in combination with much higher thermal properties and lower density.

The studies reporting the use of He for LPBF have shown that additions of He to the process gas typically leads to a more stable process with a reduction of hot spatters and fumes for Ti-6Al-4V [2] and Inconel 625 [3]. With a similar laser wavelength and using a higher laser power density compared to [2, 3], Caballero et al.[4] obtained analogous findings for 304 stainless steel. In general, it is proposed that He-processing reduces the interaction of the laser with by-products, leading to fewer fluctuations in energy input. Advanced characterization of samples produced by LPBF with He has been conducted to highlight possible differences in solidification microstructure and residual stresses. It was put in evidence that parts of standard geometries produced with He exhibit comparable grain size and orientation as their Ar counterparts. This was verified for both 316 L stainless steel [5] and Ti-6Al-4V [6] over a window of process parameters. The measurement of subsurface residual stresses by energy-dispersive diffraction highlighted that the influence of specimen's aspect ratio predominates that of the process gas type, i.e. higher aspect ratio leading to heat accumulation and thus lower residual stresses [6].

While the existence of an effect of He on the process stability is undisputable, one needs to clearly demonstrate if He influences the thermal history of the printed material. In addition, a better understanding of spatter generation mechanisms is needed to explain the previously observed differences in hot spatter generation. The in-house designed LPBF printer setup developed at the Paul Scherrer Institute (PSI) [7], permits to replicate the process in 3 D while performing ultra-fast operando X-ray diffraction and imaging. From the collected diffraction patterns and assuming that peak position only depends on thermal expansion, temperature profiles of specific phases, such as α and β phases in case of Ti-6Al-4V, can be derived. This optimal tool to assess the effect of process gas on heat dissipation was used in the present work. To observe spatter formation during LPBF, the same miniature system was employed for radiography at an imaging beamline.

Several replicator systems have been developed in recent years for dedicated use at synchrotrons to conduct ultra-fast X-ray imaging and diffraction. For example, Zhao et al.[8] used a system at the Advanced Photon Source consisting of a powder bed between two glassy carbon plates to observe the dynamic formation of the keyhole. Calta et al.[9] performed complementary observation at the Stanford Synchrotron Radiation Lightsource, Leung et al.[10] at the Diamond Light Source and Uhlmann et al.[11] at PETRA III, DESY, with systems based on the same principle. Lhuissier et al.[12] developed a different replicator allowing to perform 3 D X-ray microtomography after each printed layer and follow the evolution of defects, with a 3 D powder bed and thus closer to the real processing conditions. Still, to date, the system developed by Hocine et al.[13] is the one permitting ultra-fast operando XRD and imaging in conditions closest to the reality of the industrial process, and thus was used in the present work. Indeed, the miniaturised instrument features a 3 D powder bed and a directional gas flow over the printing area. This ensures that by-products formation and ejection are not constrained by the production volume and that heat transfers can be compared to that occurring on larger LPBF systems.

The ultra-fast operando XRD and X-ray imaging of Ti-6Al-4V during LPBF under Ar and He, completed by post-mortem evaluation of samples by high-resolution scanning electron microscopy and topography measurement brings new insights into the role of the process gas.

2. Materials and Methods

Plasma atomised Ti-6Al-4V powder of Grade 5 supplied by AP&C with spherical morphology was used. The particle size distribution was measured with a MasterSizer 3000 (Malvern Panalytical) and results provided with a D_{10} of 23 μm and D_{90} of 48 μm. This material was used to print specimens using a miniaturized LPBF system developed at PSI, with a design intended for installation at synchrotron beamlines to conduct both operando X-ray diffraction and imaging, see Figure 1. The system is introduced in further detail in the following publications [7, 13]. It is equipped with a 500 W redPOWER® continuous wave fibre laser (SPI Lasers Ltd) and a baseplate area of 11 × 11 mm^2. Square-shaped specimens with dimensions 6 × 6 mm^2 and 2 × 2 mm^2 were printed. Optimized laser parameters to achieve high density were employed as follows: layer thickness of 30 μm, hatch distance of 60 μm, scanning speed of 600 mm/s and laser power of 250 W, with a focused laser spot size of 100 μm. The scanning vectors were rotated by 90° between the consecutive layers deposited. The baseplates were machined from a large Ti-6Al-4V block produced from the same powder using an industrial LPBF system (EOS M290 from EOS GmbH) and standard parameters to ensure composition and microstructural continuity with the newly deposited material with the replicator.

Three different gases were employed to establish a protective atmosphere: pure Ar, Varigon®He50 (Linde GmbH) consisting of 50% Ar and 50% He, and pure He. The standard process condition established in Ar with a flow of 2 L/min was used as a reference. With the two other gases, the maximum gas flow achieved was 1.2 L/min, limited only by the current system design. Therefore, additional experiments under 1.2 L/min of Ar were performed for comparison.

Operando X-ray diffraction experiments were conducted at the MicroXAS beamline at the Swiss Light Source (SLS) using an X-ray energy of 12 keV. The miniaturized LPBF replicator was tilted at an angle of 15° to conduct measurements in the reflection geometry. An ultrafast single-photon counting hybrid EIGER detector developed in-house was used to record the 2 D diffraction patterns and operated at a frame rate of 20 kHz during 1 s. The 2 D images were reduced to 1 D patterns using the software package pyFAI for azimuthal integration. For an individual scanned layer, the data can be displayed by stacking the diffraction patterns, allowing to follow diffraction intensity versus angle as a function of time. The evolution of the phases within the deposited material during printing was tracked from the intensity of the recorded diffraction peaks for α/α’ and β phases. Herein, it is assumed that the peak position is mainly dependent on the thermal expansion, and the contribution from internal stresses and chemical composition are not considered. From tabulated thermal expansion coefficients [14], the temperature can be calculated from the lattice spacing. Cooling rates were derived based on the tangent of the temperature-time curves after polynomial fitting. More details on the setup and analysis procedures can be found in [7, 13].

The *operando* X-ray imaging experiments were performed at the TOmographic Microscopy and Coherent rAdiology experimenTs (TOMCAT) beamline of the SLS. The miniaturized LPBF device was mounted on a dedicated stage and tilted by 20° compared to the direction of the incoming X-ray beam. The edge of the powder bed was illuminated by a parallel X-ray beam with energies ranging between approximately 10 and 55 keV. The transmitted X-ray beam was recorded with the in-house developed GigaFRoST detector [15]. The optics consist of a custom-made microscope with 4× magnification and a high numerical aperture of 0.35, resulting in an effective pixel size of 2.75 μm. The experiments were performed at an acquisition frequency of 10 kHz with a field of view of 2.773 × 1.100 mm^2 (width × height). A scanning speed of 250 mm/s was used to capture more details of the process dynamics, and the power was decreased accordingly to 125 W to reduce the energy input. Pure Ar and pure He with a flow of 1.2 L/min were employed successively. The videos provided here depicts the process for the laser moving in the normal direction to the observation plane.

Following the prints, topography measurements of the top surface of the as-built samples were performed by confocal fusion with a SensoFar Neox system using a 10× ocular. Large maps were obtained by stitching 6 × 9 acquisitions on the 6 × 6 mm^2 surfaces, and of 3 × 3 acquisitions on the 2 × 2 mm^2 surfaces, with lateral and vertical resolutions of 6.4 μm and 1.25 nm, respectively. The data were evaluated using the software Mountains Maps to derive quantities such as the arithmetical mean height Sa, which expresses the difference in height of each point to the arithmetical mean of the surface, in absolute. High-resolution scanning electron microscopy (SEM) was also performed to identify causes of local height variations using a Zeiss Gemini 450 SEM.

The polished top surface of the printed samples were characterized by electron backscattered diffraction (EBSD) with the same Zeiss Gemini 450 SEM. The surfaces were mechanically polished with a 9 μm diamond suspension and up to a final step with a MD-Chem cloth (Struers) and a mixture of OP-S (colloidal suspension) with H_2O_2. A 2 μm step size and a 200× magnification were employed to acquire orientation maps of the XY polished top surfaces. The collected data were post-processed with HKL-Channel 5^{TM}. The parent β grains were numerically reconstructed using the MATLAB toolbox MTex based on the Burger Orientation Relationship (BOR) existing between the hexagonal α phase and the cubic β phase.

3. Results and discussions

3.1. Operando X-ray diffraction

Figure 2(a-c) displays the evolution of the diffraction patterns collected for individual scanned layers for the investigated gases. Such figures are obtained by stacking the patterns and presenting the intensity versus diffraction angle as a function of time. The corresponding temperature evolution is depicted in Figure 2(d-f). Overall the maximum cooling rates of the β phase appear similar among the tested conditions and are in the order of -0.7 to -1.2×10^6 K/s, see Table 1. In addition, the cooling rates are slightly higher in the 6 × 6 mm^2 compared to the 2 × 2 mm^2 scanned area. This is consistent with previous work [13] suggesting that higher temperatures of the β phase are retained for shorter scanning vectors.

3.2. Electron backscattered diffraction

Large area electron backscattered diffraction (EBSD) mapping was performed on the polished top surface of the printed areas. Figure 3 displays the reconstructed parent β grains with the colour code describing the local crystallographic indexing along the building direction (Z), for the areas produced under 1.2 L/min of Ar and He. Comparable maps were recorded for the other produced specimens, characterized by analogous features and from which similar conclusions could be drawn. Overall a chessboard-like pattern is distinguishable over the XY top surface for all produced areas. This is likely attributed to the 90° rotation of the scan vector between deposited layers. This pattern as well as the grain area and orientation appear rather similar among the tested atmospheres, regardless of the size of the scanned area. The analogous microstructure observed suggests that the process gas did not affect the cooling rate to the extent that would result in different grain sizes. This is consistent with the results reported in [6] for Ti-6Al-4V produced in an industrial LPBF machine. In addition, the authors also showed that no difference in terms of subsurface residual stresses exist between cuboids (5 × 5×10 mm^3) produced under Ar and He [6].

3.3. Top surface topography

Figure 4 depicts the topography measurements performed on the as-built top surface of the printed areas. One can first notice the increasing roughness values associated with the larger scanned

areas. SEM observations permit to highlight that the roughness is owing to the deposition of spatters on the top surface, which is thus more visible when the surface for redeposition increases.

It appears rather clear that the surfaces obtained with He and addition of He are more even regardless of the used gas flow, with in general lower Sa values than the Ar equivalent. It is also interesting to point out the aggravation of the surface roughness in the case of Ar when the gas flow is reduced from 2 to 1.2 L/min. Overall the results are concordant with less efficient removal of spatters under reduced Ar gas flow which redeposits on top of the scanned surface, as seen from the oxidized particle in the insert of Figure 4. In the case of He-rich atmospheres, the measurements are consistent with the findings from [2]. In this work, high-speed shadow imaging of the LPBF process under Ar and He, highlighted both a reduction of generated spatter and less concentration of these by-products at the melt pool vicinity with He. The lower Sa values of the areas printed with He are therefore attributed to less generation and thus redeposition of spatters.

As demonstrated by Chen et al.[16], surface roughness is the most determining factor limiting fatigue life of Ti-6Al-4V components built by LPBF and it also depends on the orientation of the surface to the manufacturing plane. It is therefore interesting to improve this characteristic for aerospace and medical applications. It has been shown by Molinari et al.[17] that roughness varies importantly with process parameters. And they obtained same order of magnitude of Sa value for Ti-6Al-4V (~12 μm) for the processing parameters most resembling present ones.

3.4. Operando X-ray imaging

Radiography videos were recorded while printing with pure Ar and pure He with a flow of 1.2 L/min. These are available as Supplementary Videos related to this article. Compared to shadowgraphy, radiography shows a limited indication of spatter temperature and cooling rates. However, it is the only method, to date, that permits identifying the mechanisms of spatter formation during LPBF. From the videos, several mechanisms are revealed such as the rapid entrainment of powders from the powder bed, the formation of agglomerates, and the melting of particles and spatters in the laser beam pathway. The radiography permits to capture accurately events occurring mostly in the plane of observation. In turn, the statistics of events observed for both process gas are limited. Based on the topography measurements presented above and evidence presented in the literature [2], it is highly suspected that the interaction of the laser with powder and spatters is enhanced under Ar, leading to more redeposition on the top printed surface as seen in Figure 4. Selected composite images of such interactions are presented in Figures 5 and 6. The formation of agglomerate close to the melt track, and the generation of direct melt pool ejection can be clearly depicted, as well as the melting and spheroidization of by-products crossing the beam trajectory. Such melt ejections and remelted products are occurring at high enough temperature to emit light in the visible range and are the hot spatter identified by other means such as high-speed camera and shadowgraphy. Events such as a sudden change in ejection angle of spatters were also observed by high-speed imaging [18], but not with equivalent time and spatial resolution as granted by radiography herein. A dedicated analysis of the videos and more particularly of the spatter generation is ongoing and will be presented in the future work in more detail.

4. Conclusions

While previous high-speed imaging revealed that hot spatters generated during LPBF cool faster in He, the current findings from operando XRD, with a replicator designed at PSI, highlight that He addition does not significantly promote the cooling of the high-temperature β phase for the investigated part design and process parameters. This is also reflected by the very similar EBSD inverse pole figures maps of the reconstructed parent β grains among the process gas investigated.

Topography measurement of the top surface of the printed specimen confirms that the protective Ar gas flow over the powder bed is vital to remove by-products such as spatters and condensates. As the gas flow was decreased, more particles redeposited on the powder bed and melted area. Still, it was confirmed that by using He and Ar-He mixtures, the roughness could be greatly improved. This was attributed to a reduction of hot spatter generation and redeposition. Operando X-ray imaging highlighted that these hot spatters can be produced in Ar by direct melt pool ejection, agglomeration close to the melt that is subsequently melted, and even agglomerate travelling at larger distance from the process plane that crosses the laser beam path. This indicates that the impact of He as process gas is primary on the spatter formation and spatter cooling rate, resulting in faster cooling of spatter and hence lower number of spatters that adhere to the as-built surface. This in turn results in higher process stability and better surface finish.

Acknowledgments

This work was supported by the Ulrica project (DNr 2019-05272) and conducted in the framework of the Centre for Additive Manufacturing – Metal (CAM^2), both supported by the Swedish Governmental Agency of Innovation Systems (Vinnova). The authors are also acknowledging Ola Lyckfeldt and Jonas Holmberg from RISE IVF for the PSD and topography measurements respectively. This work was further supported by the PREcision Additive Manufacturing of Precious metals Alloys (PREAMPA) project, funded by the ETH board and the Swiss watch and precious metals industry and by the Additive Manufacturing and Metallic Microstructures (AM3) project, funded by the Competence Center for Materials Science and Technology (CCMX) and the Swiss watch and precious metals industry.

References

[1] Bidare, P., Bitharas, I., Ward, R. M., Attallah, M. M., and Moore, A. J., 2018, "Laser Powder Bed Fusion at Sub-Atmospheric Pressures," Int. J. Mach. Tools Manuf., **130**–**131**(April), pp. 65–72.

[2] Pauzon, C., Hoppe, B., Pichler, T., Dubiez-Le Goff, S., Forêt, P., Nguyen, T., and Hryha, E., 2021, "Reduction of Incandescent Spatter with Helium Addition to the Process Gas during Laser Powder Bed Fusion of Ti-6Al-4V," CIRP J. Manuf. Sci. Technol., **35**, pp. 371–378.

[3] Traore, S., Schneider, M., Koutiri, I., Coste, F., Fabbro, R., Charpentier, C., Lefebvre, P., and Peyre, P., 2021, "Influence of Gas Atmosphere (Ar or He) on the Laser Powder Bed Fusion of a Ni-Based Alloy," J. Mater. Process. Tech., **288**(May 2020), p. 116851.

[4] Caballero, A., Suder, W., Chen, X., Pardal, G., and Williams, S., 2020, "Effect of Shielding Conditions on Bead Profile and Melting Behaviour in Laser Powder Bed Fusion Additive Manufacturing," Addit. Manuf., **34**(April), p. 101342.

[5] Pauzon, C., Leicht, A., Klement, U., Forêt, P., and Hryha, E., 2020, "Effect of the Process Gas and Scan Speed on the Properties and Productivity of Thin 316L Structures Produced by Laser-Powder Bed Fusion," Metall. Mater. Trans. A.

[6] Pauzon, C., Mishurova, T., Evsevleev, S., Dubiez-Le Goff, S., Murugesan, S., Bruno, G., and Hryha, E., 2021, "Residual Stresses and Porosity in Ti-6Al-4V Produced by Laser Powder Bed Fusion as a Function of Process Atmosphere and Component Design," Addit. Manuf., **47**(September), p. 102340.

[7] Hocine, S., Van Petegem, S., Frommherz, U., Tinti, G., Casati, N., Grolimund, D., and Van Swygenhoven, H., 2020, "A Miniaturized Selective Laser Melting Device for Operando X-Ray Diffraction Studies," Addit. Manuf., **34**(February), p. 101194.

[8] Zhao, C., Fezzaa, K., Cunningham, R. W., Wen, H., De Carlo, F., Chen, L., Rollett, A. D., and Sun, T., 2017, "Real-Time Monitoring of Laser Powder Bed Fusion Process Using High-Speed X-Ray Imaging

and Diffraction," Sci. Rep., **7**(1), p. 3602.

[9] Calta, N. P., Wang, J., Kiss, A. M., Martin, A. A., Depond, P. J., Guss, G. M., Thampy, V., Fong, A. Y., Weker, J. N., Stone, K. H., Tassone, C. J., Kramer, M. J., Toney, M. F., Van Buuren, A., and Matthews, M. J., 2018, "An Instrument for in Situ Time-Resolved X-Ray Imaging and Diffraction of Laser Powder Bed Fusion Additive Manufacturing Processes," Rev. Sci. Instrum., **89**(5).

[10] Leung, C. L. A., Marussi, S., Atwood, R. C., Towrie, M., Withers, P. J., and Lee, P. D., 2018, "In Situ X-Ray Imaging of Defect and Molten Pool Dynamics in Laser Additive Manufacturing," Nat. Commun., **9**(1), pp. 1–9.

[11] Uhlmann, E., Krohmer, E., Schmeiser, F., Schell, N., and Reimers, W., 2020, "A Laser Powder Bed Fusion System for in Situ X-Ray Diffraction with High-Energy Synchrotron Radiation," Rev. Sci. Instrum., **91**(7).

[12] Lhuissier, P., Bataillon, X., Maestre, C., Sijobert, J., Cabrol, E., Bertrand, P., Boller, E., Rack, A., Blandin, J. J., Salvo, L., and Martin, G., 2020, "In Situ 3D X-Ray Microtomography of Laser-Based Powder-Bed Fusion (L-PBF)—A Feasibility Study," Addit. Manuf., **34**(May).

[13] Hocine, S., Swygenhoven, H. Van, Petegem, S. Van, Sin, C., Chang, T., Maimaitiyili, T., Tinti, G., Sanchez, D. F., Grolimund, D., and Casati, N., 2020, "Operando X-Ray Diffraction during Laser 3D Printing," Mater. Today, **34**(April), pp. 30–40.

[14] Touloukian, Y. S., Kirby, R. K., Taylor, R. E., and Lee, T. Y. R., 1975, *Thermal Expansion*, Springer US, Boston.

[15] Mokso, R., Schleputz, C. M., Theidel, G., Billich, H., Schmid, E., Celcer, T., Mikuljan, G., Sala, L., Marone, F., Schlumpf, N., and Stampanoni, M., 2017, "GigaFRoST: The Gigabit Fast Readout System for Tomography," J. Synchrotron Radiat., **24**(6), pp. 1250–1259.

[16] Chen, Z., Cao, S., Wu, X., and Davies, C. H. J., 2019, *Surface Roughness and Fatigue Properties of Selective Laser Melted Ti-6Al-4V Alloy*, Elsevier Inc.

[17] Molinari, A., Ancellotti, S., Fontanari, V., Iacob, E., Luchin, V., Zappini, G., and Benedetti, M., 2022, "Effect of Process Parameters on the Surface Microgeometry of a Ti6Al4V Alloy Manufactured by Laser Powder Bed Fusion : 3D vs. 2D Characterization," Metals (Basel)., **12**.

[18] Yin, J., Wang, D., Yang, L., Wei, H., Dong, P., Ke, L., Wang, G., Zhu, H., and Zeng, X., 2019, "Correlation between Forming Quality and Spatter Dynamics in Laser Powder Bed Fusion," Addit. Manuf., **31**(September 2019), p. 100958.

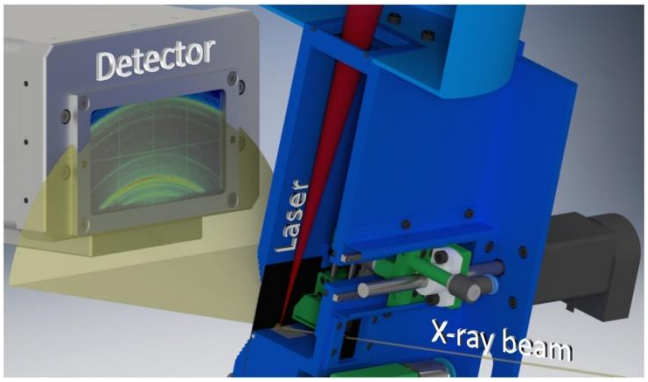

Figure 1: Diffraction geometry of the system during an operando measurement of the LPBF process. The X-ray beam enters the printer (in blue) from one side through a glassy carbon window, and is diffracted on the powder bed forming a diffraction cone collected by the high-speed detector, while the laser (red) scans the powder bed[1].

[1] Reprinted from Additive Manufacturing, Samy Hocine, Steven Van Petegem, Ulrich Frommherz, Gemma Tinti, Nicola Casati, Daniel Grolimund, Helena Van Swygenhoven, A miniaturized selective laser melting device for operando X-ray diffraction studies, 9 pages, Copyright 2020, with permission from Elsevier.

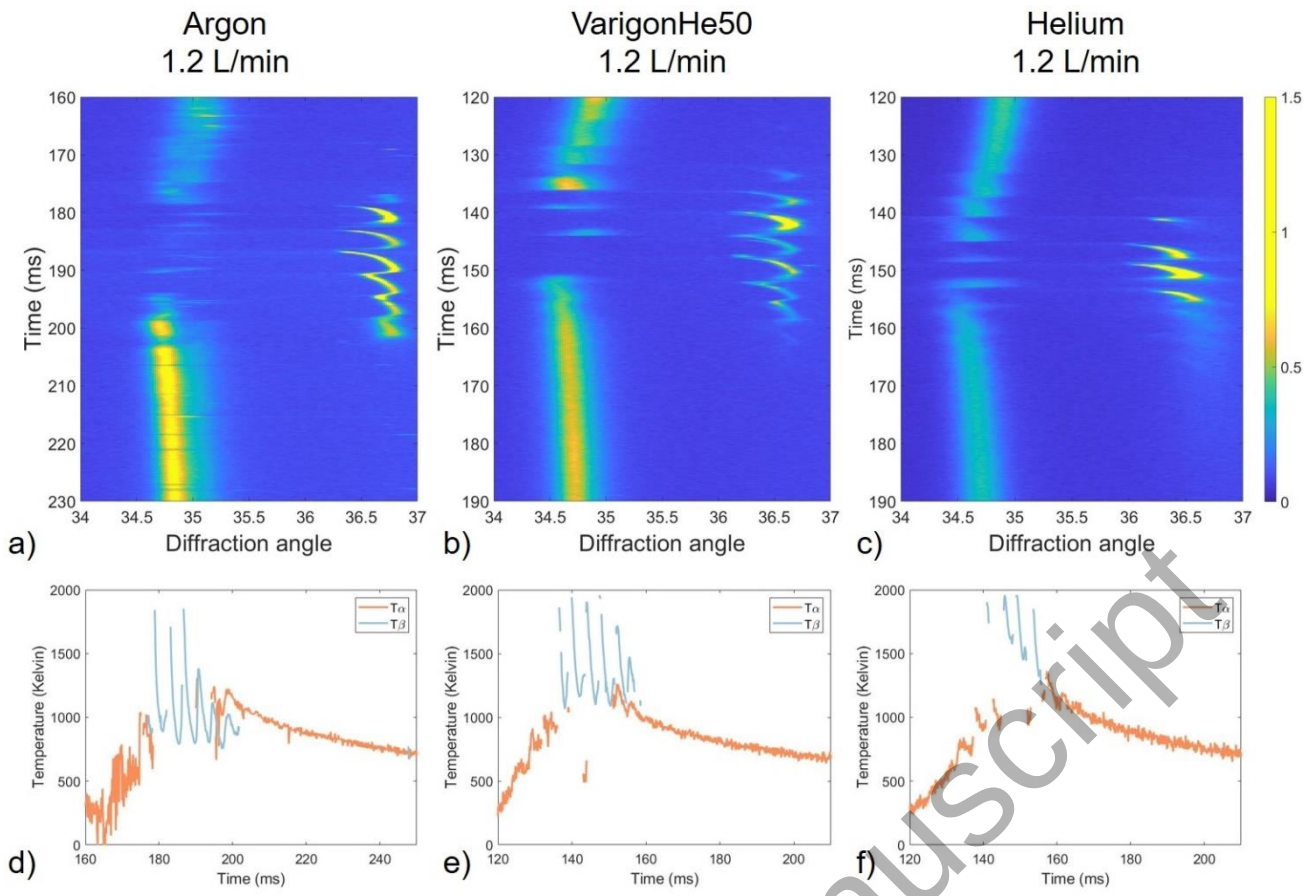

Figure 2: (a-c) Evolution of the diffraction patterns recorded during the scanning of single layers of the 6 × 6 mm^2 samples, displayed as intensity versus diffraction angle and time waterfall plot. The colour scale was capped at 1.5 counts per pixel for visibility. (d-f) Corresponding temperature evolution in the α and β phase fields.

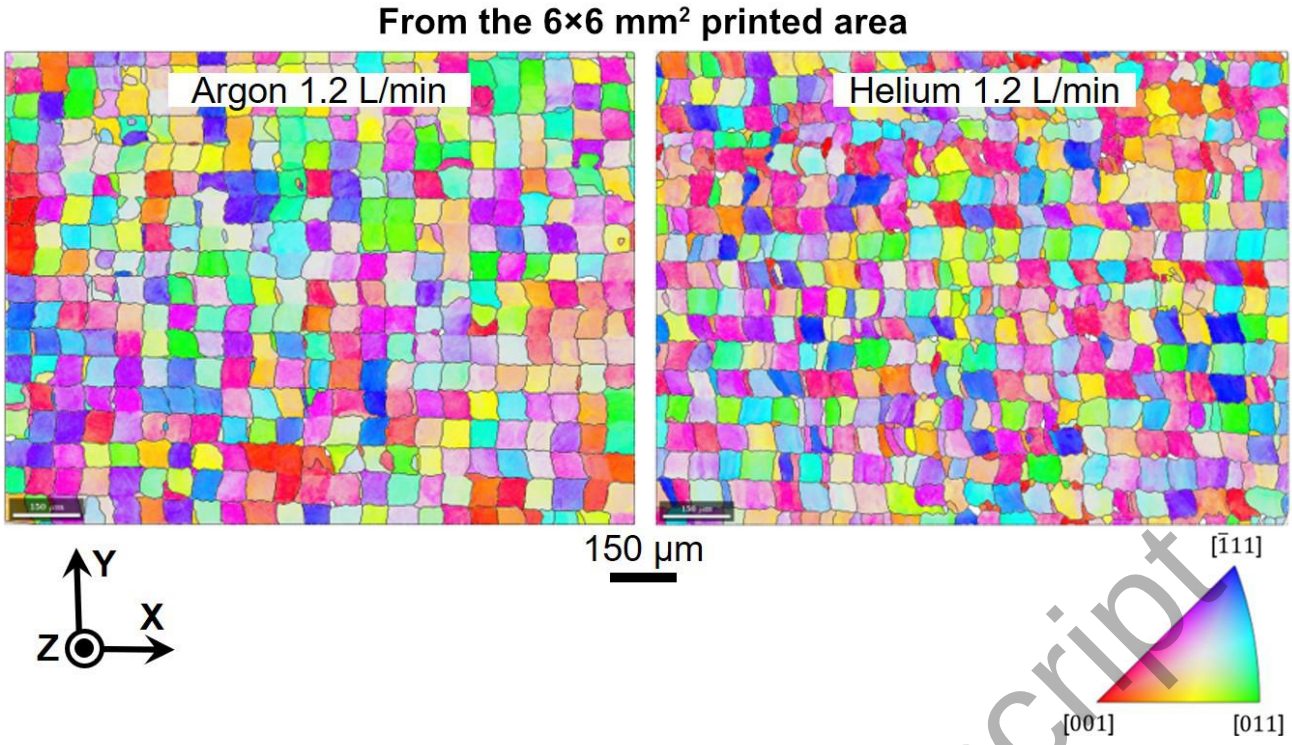

Figure 3: Extracted IPF maps of the reconstructed parent β grains in the building plane of the 6 × 6 mm^2 samples produced under Ar and He and a flow of 1.2 L/min.

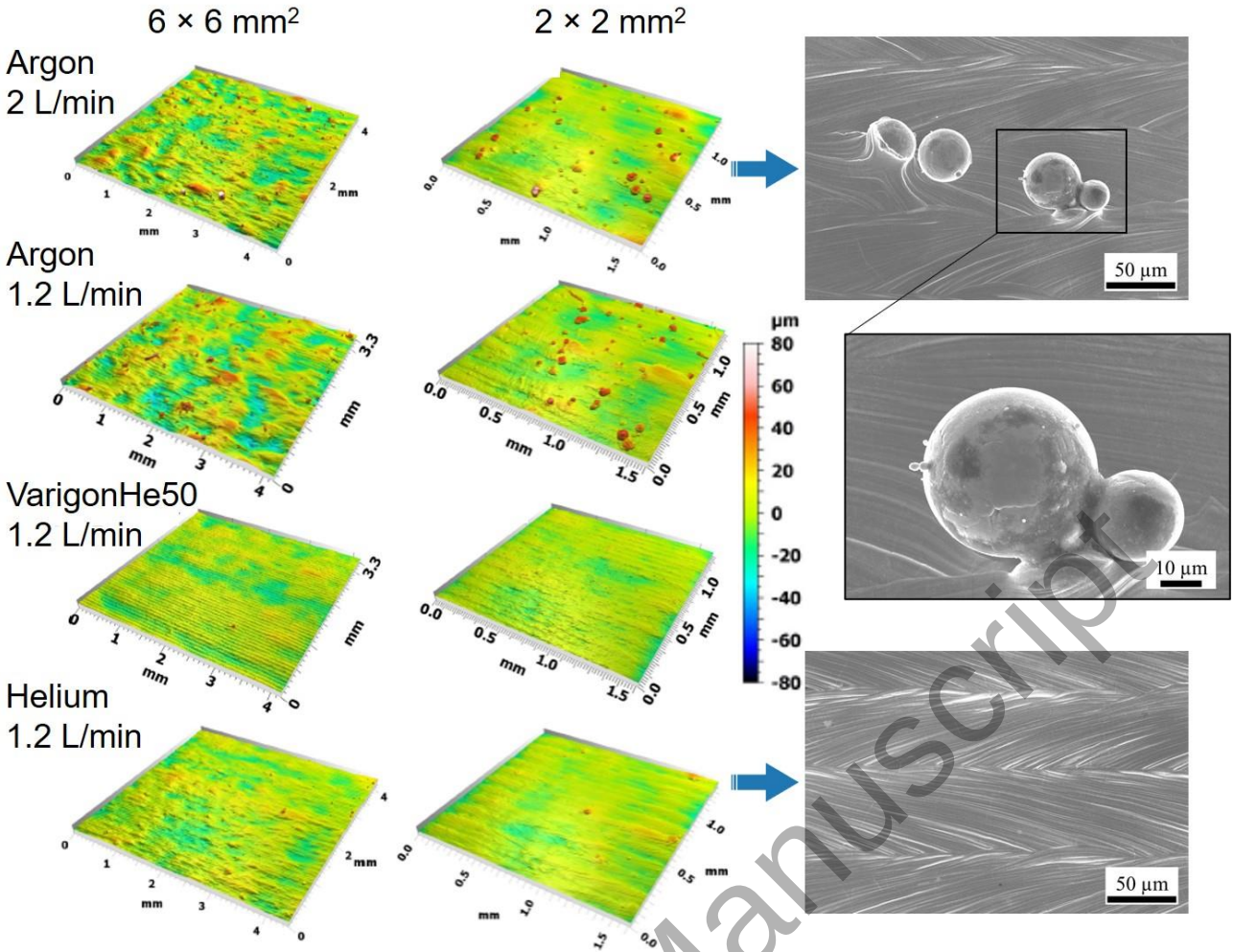

Figure 4: Topography measurements of the produced specimens with the miniature LPBF system using the confocal fusion method for the different process atmosphere conditions.

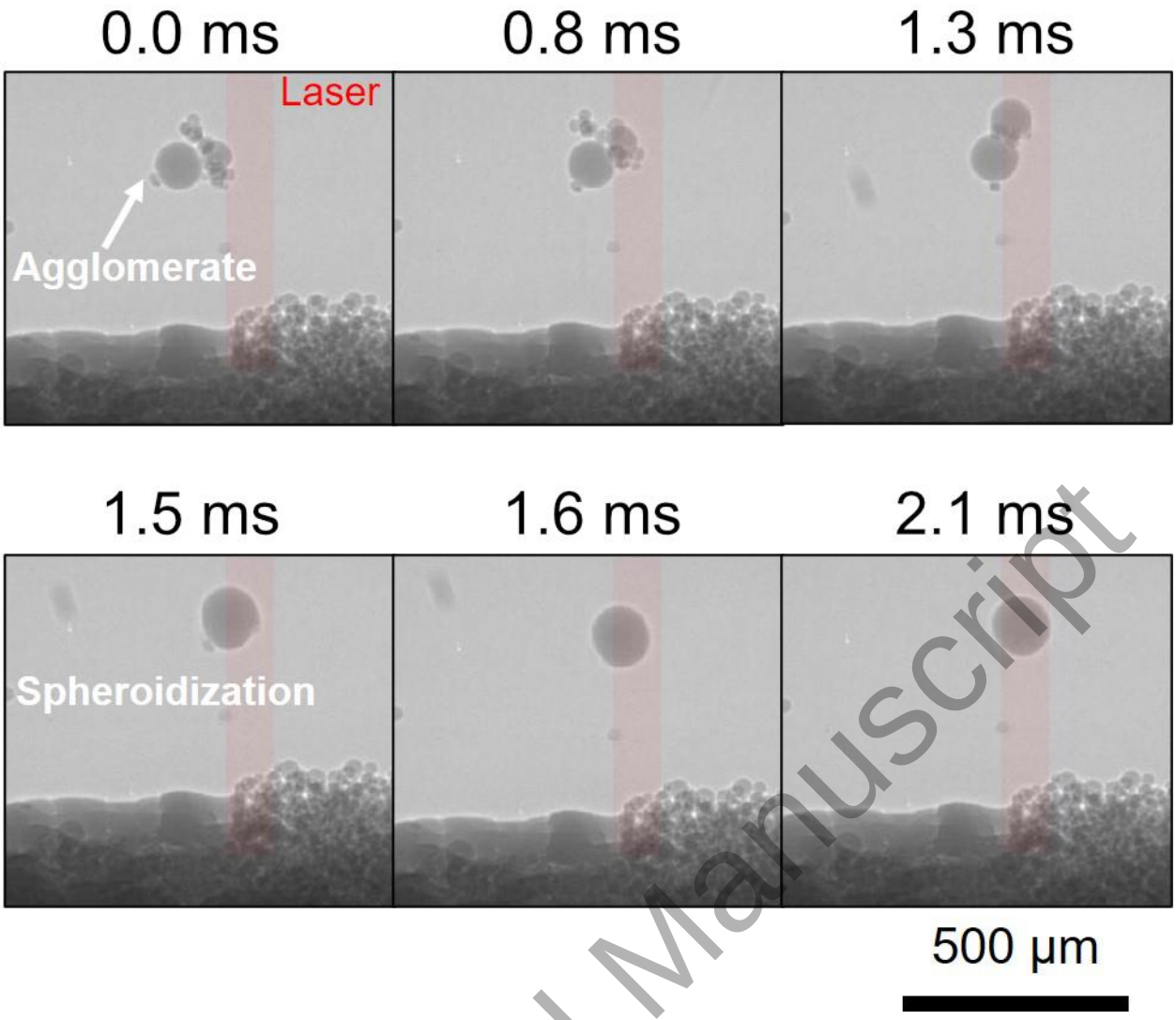

Figure 5: Composite image from the radiography experiment conducted under Ar, presenting the melting starting at 1.3 ms and spheroidization of an agglomerate as it passes through the laser beam, evidently at 1.5 ms.

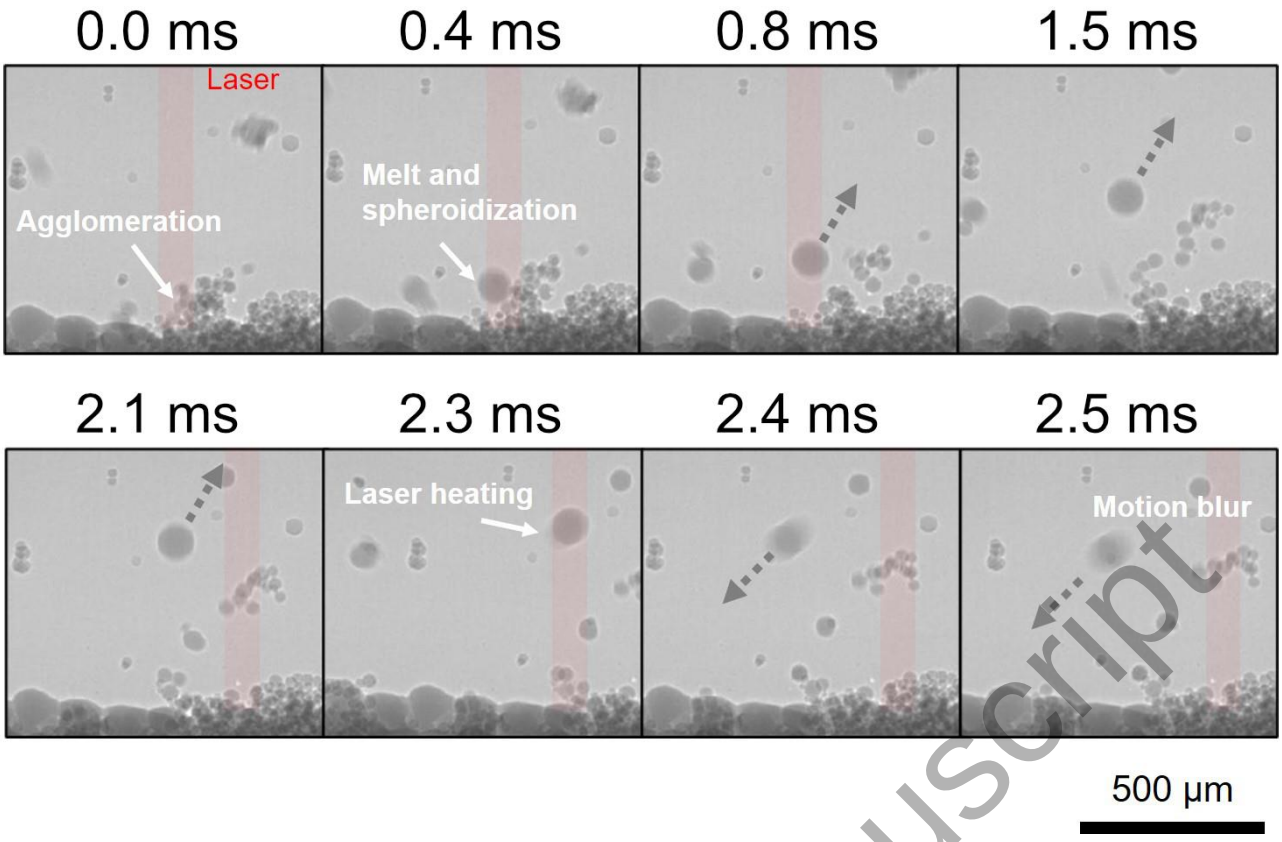

Figure 6: Composite image from radiography experiment conducted under Ar, presenting the formation of an agglomerate, its spheroidization, followed by its ejection and sudden change of direction as it is partially heated by the laser beam.

Table 1: Average of maximum cooling rate per layer in the β phase measured from the smoothen temperature profiles and computed for the two area dimensions in Ar (based on 18 layers), VarigonHe50 (5 layers) and He (17 layers).

	Average maximum cooling rates [10^3 K/s]	
Condition	**6 × 6 mm^2**	**2 × 2 mm^2**
Ar 1.2 L/min	-1197 ± 286	-939 ± 232
VarigonHe50 1.2 L/min	-1045 ± 76	-819 ± 105
He 1.2 L/min	-1196 ± 353	-703 ± 203